AIChE Journal
DOI10.1002/aic.17639

# An index to characterize gas-solid and solid-solid mixing from average volume fraction fields

Barlev R. Nagawkar[a,b], Venkata P. Kotrike[a,b], Alberto Passalacqua[a,b], Shankar Subramaniam[a,b]

[a]*Department of Mechanical Engineering, Iowa State University, Black Engineering Building, Ames, IA 50011, USA*

[b]*Center for Multiphase Flow Research and Education (CoMFRE), Iowa State University, Ames, IA, 50011, USA*

**Abstract**

A mixing index based on solid volume fraction fields is developed for gas-solid flows. Conventional mixing indices are based on particle realizations of granular mixing and are applicable to experimental data or DEM simulations. However, these indices cannot be used as-is for multi-fluid models, and an index for characterizing mixing in gas-solid flows from continuous fields is needed. The performance of the mixing index is tested in two applications. The first is a 3D simulation of the mixing of biomass and sand in a fluidized bed reactor, and the second is a 2D simulation of binary particle segregation in a fluidized bed. The simulations are performed using OpenFOAM®. The mixing index is used to quantify gas-solid mixing using solid volume fractions and solid-solid mixing using solid fractions. The formulation of conventional mixing indices is extended to be used with solid volume fractions fields, and methods for performance improvement are presented.

*Keywords*: Mixing index, gas-solid mixing, Eulerian model, computational fluid dynamics, fluidized bed

## 1. Introduction

Particle mixing and segregation are common processes used in various industries such as pharmaceutical, chemical, food, cosmetic, and ceramic industry. In the chemical industry, gas-solid mixing plays an important role when gas-solid reactions are present; for example, in chemical looping combustion[1,2]. Solid mixing is vital in the fast pyrolysis of biomass in fluidized bed reactors, where biomass mixes with sand which acts as the heat carrier[3,4]. Experimental studies have been conducted with noninvasive techniques for flow visualization to understand particle behavior within the interior of granular mixers[5–17]. With the increase in computational power, the use of computational methods




Received: May 12, 2021;Revised: Dec 27, 2021;Accepted: Jan 30, 2022

has increased over recent decades. Particle simulations based on the Discrete Element Method (DEM) and have been used to study mixing in a variety of granular mixtures[18–29]. For fluidized beds or devices at the industrial scale, with small and many particles, DEM simulations become computationally expensive because their cost scales with the number of particles. Alternatively, granular flow can be modeled using a continuum approach that obeys Eulerian conservations of mass, momentum, and energy[30,31], which only need to resolve spatial variation of averaged fields.

The multiphase computational fluid dynamic (mCFD) models are Eulerian multi-fluid models based on a random-field statistical approach[32,33] to gas-solid flows. Each phase is treated as an interpenetrating continuum defined in the Eulerian frame of reference. Phase indicator functions are random fields used to distinguish the presence of a phase $\beta$ in a realization $\omega$. For every given location in space, the indicator function tells if the given phase exists or not. If the phase exists, the local value of the indicator function is 1, and if not, it is 0. The indicator can be written as

$$I_\beta(\mathbf{x}, t; \omega) = \begin{cases} 1 & \text{if } \mathbf{x} \text{ is in phase } \beta \text{ at time } t \\ 0 & \text{if } \mathbf{x} \text{ is not in phase } \beta \text{ at time } t \end{cases}. \tag{1.1}$$

The solid volume fraction $\phi$ can be interpreted as the ensemble average of the solid phase indicator function shown in Eq. (1.2), where the angled brackets correspond to ensemble averaging:

$$\phi(\mathbf{x}, t) = \langle I_s(\mathbf{x}, t) \rangle. \tag{1.2}$$

The solid volume fraction field obeys a conservation equation similar to density in a variable density single phase fluid flow, and evolves with the phase-averaged velocity $\langle \mathbf{u}_s \rangle$ as follows:

$$\frac{\partial \phi}{\partial t} + \nabla \cdot (\phi \langle \mathbf{u}_s \rangle) = 0. \tag{1.3}$$

The solid phase-averaged velocity $\langle \mathbf{u}_s \rangle$ is defined as

$$\langle \mathbf{u}_s \rangle = \frac{\langle I_s \boldsymbol{u} \rangle}{\langle I_s \rangle}, \tag{1.4}$$

and obeys the conservation of momentum equation, which looks like the Navier-Stokes equation:

$$\begin{aligned} \frac{\partial}{\partial t}(\rho_s \phi \langle \mathbf{u}_s \rangle) \; + \; \nabla \cdot (\rho_s \phi \langle \mathbf{u}_s \rangle \langle \mathbf{u}_s \rangle) \\ = \langle I_s \rho_s \mathbf{b} \rangle \; + \; \langle \nabla \cdot I_s \boldsymbol{\tau} \rangle \; + \langle \boldsymbol{\tau} \cdot \mathbf{n} \delta\big(\mathbf{x} \; - \; \mathbf{x}^{(I)}\big) \rangle \; - \; \nabla \cdot \langle I_s \rho_s \mathbf{u}_s'' \mathbf{u}_s'' \rangle. \end{aligned} \tag{1.5}$$

The terms on the right-hand side correspond to body force, the divergence of stress, solid-gas interaction, and Reynolds stress transport. It is worth noting that, because the phases are treated as interpenetrating continua, models are needed to describe solid granular properties through kinetic theory closures for granular flows[30,34–37], frictional stress models[38–40], and a drag law for the solid-gas

interaction terms[31,41–44].

A mixing index is used to quantify the quality of solid mixing. There are over forty mixing indices proposed by various authors[45–56]. The most widely used index is Lacey's index[57]. For a monodispersed system of particles with a fraction of colored particles, the Lacey index is given by:

$$M = \frac{s_O^2 - s^2}{s_O^2 - s_R^2}, \tag{1.6}$$

where $s^2$ is the sample variance in the estimated fraction of colored particles, $s_O^2 = pq$ is the variance of the completely segregated mixture, $s_R^2 = pq/n$ is the variance of a perfect mixture with $n$ particles in the sample. The probability of finding colored particles is denoted $p$, and $q = (1-p)$ is the probability of finding uncolored particles. The Lacey index gives the ratio of how much mixing has occurred to how much could occur. There are several variants of the Lacey index, such as the Kramer[58] and Rose[45,48] indices, that use the standard deviation instead of the variance. Mixing time is often studies with the mixing index, and few studies have developed a relation to quantify the mixing time[51,52,56,59]. Mixing has also been studied considering granular energy and velocity variances[29,60,61].

Characterization of mixing in a particle realization is different from characterizing it in an averaged field representation. Most mixing indices are based on particle data obtained from either experiments or discrete element method simulations[47,48,53,54,56,62]. For an extensive review of mixing indices, we refer the reader to the review article of Bhalode and Ierapetritou[56]. They have classified various indices into three categories, namely, variance-based, distance-based, and contact-based. These methods correspond to a realization of particle positions. However, multiphase computational fluid dynamics of gas-solid flow are based on averaged field representations. The question of the applicability of variance-based mixing indices, which were formulated for a realization of particle configuration and are applied to samples of particles, is then not straightforward. The distance-based and contact-based mixing indices require particle locations and cannot be applied to mCFD. In contrast, mixing in multiphase CFD is based on average volume fraction fields, and an index must be based on continuous fields defined on a grid, which would be a new category of mixing indices. Although the Lacey index has been adapted and used in mCFD of gas-solid flows[52], many open questions remain about its implementation and interpretation. For instance, Godlieb et al.[52] show that there are issues of grid dependence for small sampling volumes.

The term grid-independence is used in the context of computing a mixing index, and it should not be confused with mesh convergence in computational fluid dynamics. A mesh convergence study in CFD

involves performing the same computation on various mesh sizes to determine a reasonable mesh resolution with low discretization error. On the other hand, establishing grid independence of a mixing index would involve calculating a mixing index on different grid sizes mapped from a single CFD simulation. To understand these criteria, relevant length scales need to be addressed. There are three characteristic length scales: physical, computational, and sampling.

The first length scale corresponds to the solid volume fraction field itself. If we take the solid volume fraction $\phi$ and the gradient of the solid volume fraction $\nabla\phi$ we can define a length scale as

$$\ell_\phi = \frac{\phi}{|\nabla\phi|}. \tag{1.7}$$

The minimum of the length scale $\ell_\phi$ defines the smallest length scale encountered in the entire domain. For a bi-disperse problem, we have three physical length scales: the length scale $\ell_\phi$, the length scale $\ell_{\phi_A}$ corresponding to the solid volume fraction of particle A, and the length scale $\ell_{\phi_B}$ corresponding to that of particle B.

Multiphase CFD simulations are performed on a computational mesh. In the finite volume method, the mesh is composed of discrete cell volumes, and a grid size $h$ can be associated to the mesh. This mesh spacing is the computational length scale. The mixing index can be computed from the solid volume fractions at each cell center directly using computational cells from the CFD simulations. However, the solid volume fraction fields can also be sampled over a sampling volume with volume $\mathcal{V}_s$. The third length scale can be associated with this sampling volume and can be written as

$$\ell_s = \mathcal{V}_s^{1/3}. \tag{1.8}$$

Given the three scales, we can say that grid-independent mixing results require a sampling volume greater than the computational grid spacing and smaller than the minimum of the physical solid fraction length scales. If the condition

$$h \leq \ell_s < \min\left(\ell_\phi, \ell_{\phi_A}, \ell_{\phi_B}\right) \tag{1.9}$$

is met, we can expect grid-independent mixing results if the mixing index is appropriately defined. We can also make the sampling volume length scale larger than the spatial variation of the solid volume fraction averaged fields, as follows:

$$\ell_s > \min\left(\ell_\phi, \ell_{\phi_A}, \ell_{\phi_B}\right). \tag{1.10}$$

If we choose sampling volumes larger than the smallest physical length scale, mixing results will vary with respect to the size of the sampling volume, and we will have scale-dependent mixing.

The objective of this article is to introduce a new mixing index based on solid volume fraction fields. Two types of mixing indices are introduced in Section 2: one to quantify gas-solid mixing, and the other for solid-solid mixing. We then apply these indices to two applications in sections 3 and 4. The first application is cold flow simulations of a biomass fluidized bed reactor, and the second is a study of segregation of two types of particles in a fluidized bed. Multi-fluid simulations were performed using OpenFOAM[63,64] and the relevant equations are given in Appendix A. We see in Fig. 6 and Fig. 8, that the new mixing index helps discriminate mixing between two designs of the biomass fluidized bed reactors. Also, we see from Fig. 10 that the new index improves the performance of an existing global index. An important performance characteristic, sensitivity, is introduced in section 5 and the new mixing indices are shown to have tunable sensitivity.

## 2. Mixing index formulation

The mixing indices for gas-solid and solid-solid mixing are derived in this section. The index for gas-solid mixing is based on the particle volume fraction fields, and the index for solid-solid mixing is based on solid fraction fields. In a polydisperse system of particles, the *solid fraction* of a particle species is defined as its volume fraction divided by the total particle volume fraction. The idea of the new mixing indices is analogous to the mixture fraction that arises in single-phase mixing of fuel and oxidizer in the combustion problem. The new mixing indices *linearly map the solid volume fractions field and the solid fraction field between 0 and 1*, where the perfectly mixed state is set to 0.5 at all grid locations. The global average of the solid volume fraction and the solid fraction will always map to 0.5. By doing so, the dependency on global averages is eliminated. Both indices are functions of space and time and will be used to identify regions of rich and lean mixing. Hence, these new indices can be classified as *local mixing indices*.

### *2.1. Local mixing index*

Consider a bi-dispersed system with $\langle N \rangle$ particles, with particles of type $A$ and $B$. Let $\langle N_A \rangle$ and $\langle N_B \rangle$ be the average number of particles of $A$ and $B$ respectively, such that $\langle N \rangle = \langle N_A \rangle + \langle N_B \rangle$. The global average number density for a given type of particles are:

$$\bar{n}_A = \frac{\langle N_A \rangle}{V}, \qquad \bar{n}_B = \frac{\langle N_B \rangle}{V}, \tag{2.1}$$

where $V$ is the volume of the domain. The global average volume fractions are given as

$$\bar{\phi}_A = \frac{\pi d_A^3}{6}\bar{n}_A, \qquad \bar{\phi}_B = \frac{\pi d_B^3}{6}\bar{n}_B, \tag{2.2}$$

where $d_A$ and $d_B$ are the particle diameter of type $A$ and type $B$ particles, respectively. Perfect local mixing occurs when the local number densities match the global average number densities, that is, $n(x,t) = \bar{n}$ and $n_A(x,t) = \bar{n}_A$, or if the local volume fraction $\phi(x,t) = \bar{\phi}$, and $\phi_A(x,t) = \bar{\phi}_A$.

*2.1.1. Local mixing of particles in air*

The volume fraction $\phi(x,t)$ of the particles can vary from zero to the maximum packing limit. The local mixing index $M_\emptyset$ provides a linear scaling of the volume fraction field from 0 to 1. A value of 0.5 corresponds to the global average volume fraction $\overline{\phi}$, and values of $0 < M_\emptyset < 0.5$ define a lean mixture and for values $0.5 < M_\emptyset < 1$ define a rich mixture, analogous to the mixture fraction in combustion. We can then write:

$$M_\emptyset(x,t) = \begin{cases} a_1\phi + b_1, & 0 \le \phi < \bar{\phi} \\ a_2\phi + b_2, & \bar{\phi} \le \phi \le \phi_{max} \end{cases} \tag{2.3}$$

where $\phi_{max}$ is the maximum packing fraction for solids in the bi-dispersed system, and the coefficients $a_1, b_1, a_2$ and $b_2$ can be found using the following conditions on $M_\emptyset$

$$\begin{aligned} \phi &= 0\,, & M_\emptyset &= 0, \\ \phi &= \bar{\phi}\,, & M_\emptyset &= 0.5, \\ \phi &= \phi_{max}\,, & M_\emptyset &= 1. \end{aligned} \tag{2.4}$$

Using the above conditions to determine the values of coefficients in Eq. (2.3) gives the following expression for the local mixing index of solids in a gas-solid mixture:

$$M_\emptyset(x,t) = \begin{cases} \dfrac{\phi}{2\bar{\phi}}, & 0 \le \phi < \bar{\phi} \\ \dfrac{3}{4} + \dfrac{1}{4}\left(\dfrac{2\phi - (\phi_{max} + \bar{\phi})}{\phi_{max} - \bar{\phi}}\right), & \bar{\phi} \le \phi \le \phi_{max} \end{cases}. \tag{2.5}$$

The index in Eq. (2.5) provides the richness of the solid particle phase and can be called the *richness index*.

*2.1.2. Local mixing of particles in a mixture of particles*

In order to characterize solid-solid mixing, the solid fraction, which is the ratio of volume fraction of particles of type A to the total volume fraction of particles

$$\xi_A(x,t) = \frac{\phi_A(x,t)}{\phi(x,t)}, \tag{2.6}$$

is the relevant quantity on which the local mixing index should be defined. A value of 0 corresponds to a region with no $A$ type particles, and a value 1 corresponds to a region of only particles A. The global average solid fraction is given by:

$$\bar{\xi}_A = \overline{\left(\frac{\phi_A}{\phi}\right)}. \tag{2.7}$$

The local solid-solid mixing index $M_\xi$ is defined between 0 and 1, where a value of 0.5 corresponds to the global average solid fraction $\bar{\xi}$. For values $0 < M_\xi < 0.5$ the mixture is defined as lean, and for values $0.5 < M_\xi < 1$ as rich in $A$ particles. The local solid-solid mixing index for particles of type $A$, can be written as

$$M_{\xi_A}(x,t) = \begin{cases} c_1\xi_A + d_1, & 0 \le \xi_A < \bar{\xi}_A \\ c_2\xi_A + d_2, & \bar{\xi}_A \le \xi_A \le 1 \end{cases}, \tag{2.8}$$

where the coefficients $c_1$, $d_1$, $c_2$, and $d_2$ can be found by using the following conditions:

$$\begin{aligned} \xi_A &= 0\,, & M_{\xi_A} &= 0, \\ \xi_A &= \bar{\xi}_A\,, & M_{\xi_A} &= 0.5, \\ \xi_A &= 1\,, & M_{\xi_A} &= 1. \end{aligned} \tag{2.9}$$

From Eq. (2.8) we get the following expression for the local solid-solid mixing index:

$$M_{\xi_A}(x,t) = \begin{cases} \dfrac{\xi_A}{2\bar{\xi}_A}, & 0 \le \xi_A < \bar{\xi}_A \\ 1 - \dfrac{1}{2}\left(\dfrac{1-\xi_A}{1-\bar{\xi}_A}\right), & \bar{\xi}_A \le \xi_A \le 1 \end{cases}. \tag{2.10}$$

*2.2. Global mixing index*

The Lacey and Rose indices are applied to particle configurations using particle number fraction and provide a single value of mixing for the system as a whole. These indices can be classified as global mixing indices. Here we demonstrate the use of these indices with solid volume fraction and solid fraction fields. Note that this extension may not respect all aspects of the analysis underlying the development of these indices, and applicability of these variance-based indices explored in Appendix D. The global mixing index is scaled from 0 to 1, where a value of 0 denotes an unmixed state, and a value of 1 defines a perfectly mixed state. The form of the global indices remains the same as Lacey's or Rose's, but the standard deviations are computed on the solid volume fraction or the solid fraction. Here we use the Rose formulation to demonstrate the use of the index.

The standard deviation of volume fraction is used to define the global mixing of particles in air $M_{G,\phi}$, and it is given by:

$$M_{G,\phi} = 1 - \frac{\sigma_\phi}{\sigma_o}, \tag{2.11}$$

where $\sigma_\phi$ is the standard deviation of the current state, and $\sigma_o$ is the standard deviation of the unmixed state, defined as follows:

$$\sigma_\phi = \sqrt{\frac{\sum(\phi - \bar{\phi})^2}{N}}, \qquad \sigma_o = \sqrt{\bar{\phi}(1 - \bar{\phi})}. \tag{2.12}$$

Similarly, the global mixing index for solids of type A in a mixture of solids given by $M_{G,A}$ is defined as:

$$M_{G,\xi A} = 1 - \frac{\sigma_{\xi A}}{\sigma_{\xi o}}. \tag{2.13}$$

The standard deviation $\sigma_{\xi A}$ of the current state and that of perfectly mixing state, $\sigma_{\xi o}$, are given, respectively, by:

$$\sigma_{\xi A} = \sqrt{\frac{\sum\left(\xi_A - \bar{\xi}_A\right)^2}{N}}, \qquad \sigma_{\xi o} = \sqrt{\bar{\xi}_A\left(1 - \bar{\xi}_A\right)}. \tag{2.14}$$

A global mixing index value of 0 corresponds to an unmixed system, and a value of 1 corresponds to a well-mixed system.

## 3. Mixing of biomass and sand in fast pyrolysis

Heat transfer is a bottleneck for scale-up in conventional biomass fast pyrolysis[65,66]. Autothermal pyrolysis addresses this limitation by allowing for partial oxidation of pyrolysis products, which are exothermic reactions that provide heat for the endothermic reactions such as devolatilization[65,67]. In autothermal pyrolysis, a mixture of nitrogen and air is used as the fluidizing gas. Air is used to introduce small amounts of oxygen for char combustion, a significant contributor to the heat for the process. For the ideal performance of autothermal pyrolyzers, the retention of char in the bed is essential for the reaction with oxygen. At the same time, the quick release of volatile gases from biomass is vital for bio-oil yield. Therefore, the quality of biomass mixing in autothermal pyrolysis can have a

significant impact on yield. The height of the injection point of the biomass in the reactor could play a role in the mixing and subsequently influence yield.

In this section, we look at the mixing of biomass in a lab-scale fluidized bed reactor. Biomass is injected using an auger into the reactor, where it mixes with sand. The location of the injection points may influence how biomass and sand mix. Two injection locations are selected for this study, and cold flow simulations of biomass and sand are carried out. The simulation setup and mesh convergence study are first presented, and the mixing indices derived in section 2 are applied to the two designs.

*3.1. Simulation setup*

The fluidized bed reactor is 3.81 cm in diameter, with a height of 42.7 cm. A schematic diagram representing the computational domain is shown in Fig. 1. Silica sand of size 600 μm and density 2650 $kg/m^3$ is initialized until a height of 10.5 cm from the bottom of the bed. Fluidizing gas enters the domain from the bottom of the bed at a rate of 20 SLPM. A combination of air and biomass particles of size 1587 μm and density 700 $kg/m^3$ is fed with an auger screw at a rate of 1 kg/h. The auger screw geometry is simplified as a cylindrical obstruction, as shown in Fig. 1.

Two designs with different locations of the biomass feeder inlet, as shown in Fig. 1, were considered to study the effect on the mixing of biomass inside the fluidized bed. The position of the biomass inlet was 2.5 cm, well within the fluidized bed, for design 1 and 8.5 cm, underneath the freeboard, for design 2. Biomass and air are injected into the fluidized bed reactor for 10 s. Then injection is ceased, and the simulation is continued to 15 s.

Three-dimensional simulations of the fluidized bed reactor were done using the Eulerian multi-fluid solver in OpenFOAM[63,64]. A description of the Euler-Euler multi-fluid model with kinetic theory closures for polydisperse granular phases used is given in Appendix A. Gradients were calculated with a second order least-square method, and the a second order scheme with Sweby limiter[68] was used for the divergence terms. The superficial inlet velocity boundary conditions were used for air and biomass at the respective inlets, and a pressure inlet-outlet condition was used at the outlet boundary. A no-slip wall boundary condition was used for the gas phase velocity, and the Johnson and Jackson[38] particle slip were used for the velocities of the solid phases. The velocity of sand and biomass were set to zero at the inlet at the bottom of the fluidized bed. A Neumann boundary condition was prescribed at the wall for the volume fractions of each phase. The solid phase volume fractions were set to zero at the gas inlet and that of biomass at the biomass-inlet was set to 0.55. A fixed value for

air volume fraction of 1 and 0.45 were used at the gas and biomass inlet, respectively. The Johnson and Jackson boundary condition was used for granular energy at the wall for the solid phases. The simulation was isothermal, at a fixed temperature of 300 K.

*3.2. Mesh convergence*

The block meshing technique in OpenFOAM was used to generate a hexahedral mesh. The mesh of the cross-section of the reactor and the injection point is shown in Fig. 2. Mesh refinements were made near the wall and inlet auger. A mesh convergence study was carried out with the four mesh sizes listed in Table 1. The mesh size was calculated as[69]

$$h = \left[\frac{1}{\mathrm{N}}\sum_{i=1}^{\mathrm{N}}(\Delta V_i)\right]^{1/3}. \tag{3.1}$$

The mesh convergence study was done on time-averaged quantities. Relevant quantities for each phase were time-averaged from 2 to 10 s. The first couple of seconds were not included in the time-average to remove the impact of the initial transient condition. The remaining 8 s were found to be adequate to obtain converged mean flow fields. Initially the bed is stationary, and we allow some time for the flow to develop to a quasi-steady state. The duration for time-averaging was determined by computing the relative error in the moving average of the total solid volume fraction field.

The relative error and fine grid convergence index (GCI)[69] were computed from the Rose index applied to meshes 1, 2 and 3 from Table 1 and are presented in Table 2. Time-averaged solid volume fractions fields of sand and biomass were used. While the grid convergence index of biomass volume fraction is low, as show in Table 2, it has oscillatory convergence. The GCI for the biomass volume fraction is 0.6%, but the value of the mixing index increases from mesh 1 to 2 and then deceases from mesh 2 to 3.

In addition to the mesh convergence study, the $L^2$ norm of the true error, which is the absolute difference of the result from the best solution, was computed and plotted in Fig. 3. The true error of time-averaged solid volume fraction fields was computed for meshes 2,3 and 4 compared to the finest mesh 1. The order of convergence for the sand volume fraction is slightly above one, and that of biomass is less than 1. The second finest mesh (mesh 2) with 551,381 cells was chosen for the mixing index study.

*3.3. Local mixing*

Biomass being the lighter particle tends to float on top of the bed, and this is seen in the volume fraction plots in Fig. 4 and Fig. 5. Biomass is more concentrated at the top of the bed for Design 2 than it is for Design 1. At 5 s, the biomass is evenly distributed for Design 1 but is more concentrated towards the top of the bed at 10 s. For Design 2, the biomass remains at the top of the bed at 5 s and gets concentrated further as it is injected into the reactor.

Evenly distributed dense sand volume fraction fields are observed for Design 1 at 5 s, and moderately dense sand is observed between the middle and top portion of the bed at 10 s. Unlike Design 1, the presence of bubbles with a low concentration of sand are seen in Design 2, which grow as they move up through the bed. The biomass inlet auger obstructs the flow in Design 1 and prevents this feature, as observed in Design 2. The total particle fraction is the sum of the biomass and sand volume fractions, where the dense regions can be observed for volume fractions above 0.6.

The quality of gas-solid mixing can be quantified by applying the richness index $M_{\emptyset}$ to the total particle volume fraction. The richness index is applied to both designs at 5 s and 10 s and shown in Fig. 6. The richness index linearly scales the volume fraction ranging between 0 and maximum packing fraction $\alpha_{max}$ to 0 and 1, with 0.5 corresponding to the global average of the total volume fraction, the well-mixed state. As the bed is fluidized, the gas rises through the bed forming a relatively even distributed concentration of particles on Design 1 but successive densely packed and dilute zones of particle for Design 2 as seen in Fig 6. At 5 s, only dense regions are seen right above and at the injection inlet of the biomass auger in Design 1. As the process continues, a less dense region of particles is seen between the middle and top portion of the bed at 10s, which is attributed to the slight bed expansion. Under the biomass feeder, which is an obstruction in the fluidized bed, lean pockets with few particles are observed at both 5 and 10 s in Design 1. The bubble regions in Design 2 are enhanced by the Richness Index in contrast to the total volume fraction fields shown in Fig. 4 and Fig. 5. Higher gradients are observed below the bubble regions compared to the top portion of the bubble.

The solid mixing index can be applied to the solid fraction of biomass and sand. The solid fractions of biomass for both designs at 5 and 10 s are shown in Fig. 7. A small fraction of biomass can be seen at 5 s, and higher biomass fractions can be seen towards the top of the bed at 10 s. In the lean regions above the bed, a more significant proportion of biomass is observed for Design 2 than for Design 1, at 10s.

To quantify the quality of solid mixing, the solid mixing index $M_\xi$ is applied to the solid fraction fields. The solid-solid mixing index is applied to the solid fraction fields of biomass $\xi_A$ for both designs at 5 and 10 s, as shown in Fig. 8.

A mixing index of 0.5 corresponds to the global average solid fraction, representing a well-mixed state. A higher proportion of well-mixed biomass is seen around the biomass feeder at 5 s than it is at 10 s for Design 1. The biomass is better mixed at 10 s between the middle and top section of the bed. Note that the region at the top at 5 s has no biomass or sand in Design 1, which means that the solid volume fractions for both solid phases are zero in this region, and the solid fraction is undefined. Consequently, the mixing index in such areas is not defined. Solid fractions and the solid mixing index were clipped in Fig. 7 and Fig. 8, respectively, and replaced with a solid color to show the domain. At the bottom of Design 2, almost no biomass is present at 5 s and 10 s, which is primarily collected towards the top. Regions of $M_{\xi_A} > 0.5$ and $M_{\xi_A} < 0.5$ are seen at 10 s for Design 2, clearly indicating non-mixedness of biomass with sand. However, at 5 s, the top of the bed shows good mixing of biomass and sand. The biomass segregates from the sand as it is injected into the bed in Design 2. The region corresponding to a mixing index of 0.5 is larger in Design 1 than in Design 2; consequently, mixing in Design 1 is better than in Design 2.

### *3.4. Global mixing*

We now compare global indices based on the solid fraction to characterize solid-solid mixing. The Rose mixing index, $M_{G,\xi A}$ from Eq. (2.13), is applied to biomass solid fraction fields $\xi_A$ to quantify the overall solid-solid mixing of the two designs. The performance of few other variance-based mixing indices was studied and are presented in Appendix D, where we apply these indices to the volume fraction fields of biomass, $\phi_A$. Here we have chosen to restrict the analysis to solid-solid mixing.

The solid fraction of biomass is computed from 1 s to 10 s at intervals of 1 s. The mixing index is applied to the biomass solid fraction and plotted with time, as shown in Fig. 9. The plot is supplemented with biomass volume fraction fields $\phi_A$ at 3 s, 7 s, and 10 s for both designs. Here a global mixing index of 1 corresponds to a perfectly mixed system. The plot in Fig. 9 shows that the system is well mixed early in the injection stage for both designs. The mixing improves until 3 s in Design 1 and then segregates around 4 s. However, the mixing in Design 2 segregates until 3 s, then remains almost constant until 8 s, then segregates further until 10 s. From the instantaneous volume fraction plots, the biomass is evenly distributed in Design 1 at 3 s. As the biomass is injected into the

bed, it begins to segregate from the sand and collects at the top at 7s, and furthermore so until 10 s. The trend is captured by the global index plot. In Design 2, the biomass is collected at the top at 3 s, and some amount of the biomass moves down towards the middle of the bed at 7 s. However, the mixing index at these times is roughly the same. The concentration of the biomass at the top increases further in Design 2, which explains the drop in the quality of mixing until 10s. While the overall mixing in Design 1 is slightly better than that of Design 2, the biomass is much more segregated at 10s for Design 2 than for Design 1.

We now compare global indices based on the new mixing indices introduced in this work. We can apply the same formulation using the scaled local solid mixing index $M_{\xi_A}$. The Rose formulation applied to the local solid mixing index in time is plotted in Fig. 10 and supplemented with the same biomass volume fraction fields $\phi_A$ shown in Fig. 9. It can be seen that the sensitivity of global mixing is enhanced by the local mixing index. The difference between the quality of mixing in both designs is more significant for the index computed on the local solid-solid mixing $M_{\xi_A}$ than that computed on the solid fraction $\xi_A$. In addition, a clear improvement is seen in the performance of the index at the initial times of biomass injection. As biomass is injected into the bed, we expect that the quality of mixing of biomass and sand improves with time relative to the initial time of injection. The mixing improves dramatically for Design 1 until 3 s, and then slowly segregates as the biomass collects at the top of the bed. The mixing gradually improves in Design 2, but then segregates after 8 s. From the volume fraction fields shown in the plot, Design 1 follows a similar trend. At 3 s the biomass is relatively more evenly distributed and then collects at the top and continues to do so until 10s. Unlike the global index computed on the solid fraction fields, better mixing is seen at 7 s compared to at 3 s from the global index calculated based on the local mixing index for Design 2. At 7 s, biomass has moved further below the injection auger. At 10 s, the mixing quality reduces, as seen in Fig. 9.

The local mixing indices derived in this article were used to compare the performance of two designs of a fluidized bed reactor for fast pyrolysis of biomass. A mesh-convergent grid was determined for the CFD simulations, and the sampling for the mixing study was done using the same. The richness index $M_\phi$ applied to the total solid volume fraction in Fig. 6, shows the spatial quality of gas-solid mixing. The biomass solid fraction fields $\xi_A$ were computed, and the solid mixing index $M_{\xi_A}$ was used to quantify solid-solid mixing. As shown in Fig. 8, biomass and sand are more segregated at 10 s. The new mixing indices provide a powerful tool to identify regions of rich and lean mixing. The Rose index was used to quantify the mixing of the system for the two designs. We found that the global index

applied to the solid fraction fields $\xi_A$ is insensitive to the initial state of injection, and the performance of the index is enhanced by applying it to the local solid mixing index field $M_{\xi_A}$. From this study, Design 1 was found to be a better choice over Design 2.

## 4. Segregation in bi-disperse flows

Segregation of bi-disperse gas-solid mixtures is another problem that can be studied using mixing indices. In the biomass problem, we had two types of solid particles, biomass and sand, that were initially unmixed. Biomass was injected, and the quality of mixing was quantified. In the segregation problem, we start with a bi-disperse system of particles that are perfectly mixed in a fluidized bed. The binary mixture consists of silica sand and glass beads, and their properties are described in Table 3[70]. The particles are classified as jetsam and flotsam, where the particles that are prone to sink to the bottom of the bed are referred to as jetsam, while those that float at the top are referred to as flotsam. Both types of particles have similar densities, but the particle sizes are different. The silica sand is smaller in size and will tend to float while the glass beads will settle to the bottom of the bed.

### *4.1. Computational setup*

The simulations were done on a two-dimensional rectangular domain using the same multi-fluid model, as described in Appendix A. The domain of the fluidized bed is 0.12 m wide and has a height of 1 m and is shown in Fig. 11. The bed was initialized up to a height of 0.4 m with equal volume fractions of 0.31 for jetsam and flotsam particles each. Air is injected from the bottom of the bed with a uniform velocity of 0.1 $\mathrm{m/s}$. The same schemes and boundary conditions described in the previous section are used for this problem.

### *4.2. Mesh convergence*

As in the biomass case a mesh convergence study for the CFD simulations is done with 4 meshes as given in Table 4. The grids are uniform, with no additional refinement at walls. The simulations were run till 50 s and relevant quantities were time-averaged from 4 to 50 s. The initial time was excluded from the time averaging, to remove the impact of the initial transient start up condition. The duration of time averaging was determined as in the biomass simulations, and longer time-averaging of 46 s was needed to obtain converged mean flow fields. The reason could be attributed to the unsteady bubbling nature of the fluidized bed.

The Rose index based on the solid volume fraction fields was computed for the three finest meshes and are represented as $\emptyset_i$ in Table 5, where $i$ goes from 1 to 3 corresponding finest to coarsest mesh. The index was applied to both jetsam and flotsam time averaged volume fraction fields. The estimated error and grid convergence index[69] are computed and presented in Table 5. The relative error and GCI are acceptable for both jetsam and flotsam as they are under 5%, but the apparent order $p$ is just below 1.

The $L^2$ norm of the true error is calculated and plotted in Fig. 12. The true error was calculated for the time-averaged volume fraction fields of jetsam and flotsam from meshes 2, 3 and, 4 with reference to the finest mesh 1. The order of convergence is above 1.5 for both jetsam and flotsam fields. Mesh 2 can be used for the mixing index study; however, the finest mesh 1 was chosen since the mesh size is smaller than 1 mm. A parametric study of mixing could be done where multiple CFD simulation are needed, in which case it is recommended to use mesh 2. However, here we intend to only compute a mixing index in a single case. The computation of the mixing index is inexpensive, and the finest mesh can be used.

*4.3. Local mixing*

The simulation starts with a perfectly mixed system of particles. In time the particles segregate, and the larger particles settle to the bottom of the bed. The volume fraction fields of the flotsam, jetsam, and total particles at 30 s are shown in Fig. 13. The smaller flotsam particles are richer at the top of the bed and the larger jetsam particles are rich at the bottom. Apart from the bubbles, the volume fraction of the total particles in the fluidized bed are dense ranging from 0.6 to 0.68.

The richness index is applied to the total particle volume fraction $\phi$ as shown in Fig. 14. The scaling clearly shows the bubble regions ranging from 0 to 0.2 with lean solid gas mixing and dense granular mixing regions with values ranging from 0.9 to 1. Few regions of well-mixed gas-solid mixing are observed in the bed. These regions correspond to a mixing index of 0.5 and can be seen at the bottom of the bed and around the bubbles. The mixing in this problem is skewed with rich zones of particles and lean bubble regions that are well captured by the richness index $M_\phi$.

The solid fractions $\xi_A$ can be computed for flotsam particles from Eq. (2.6). These are computed and shown in Fig. 15. The bubbles are no longer visible as the particle volume fractions in the bubble are small but non-zero. The particle volume fractions in the bubbles are of the order 0.01, and the solid fraction computes the relative proportion of a type or particles in a mixture of particles. The top of

the bed has no particles present, and these regions were clipped. The solid mixing index is calculated on these solid fraction fields and given in Fig. 15. Note that the index is computed on the range from 0 to 1, with 0.5 corresponding to the global solid fraction average, however the figure is scaled from 0 to 0.8 to better illustrate the spatial variation.

The solid fractions and solid mixing index are nearly identical. The reason for this is that the average solid fraction of the flotsam particles is very close to 0.5. It can be shown from Eq. (2.10) that the solid mixing index $M_{\xi_A}$ reduced to $\xi_A$ for $\overline{\xi_A} = 0.5$. The problem was initialized with equal volume fractions of both jetsam and flotsam. Therefore, little scaling is observed by the local solid mixing index. The solid mixing index shows a solid mixture with a richer proportion of flotsam particles at the top than at the bottom, implying the inverse with a richer proportion of jetsam particles at the bottom of the bed.

*4.4. Global index*

As in the biomass problem, the global mixing index can be applied to the solid fraction fields $\xi_A$ and the local solid mixing index fields $M_{\xi_A}$. The Rose index was applied to these fields for every 5 s from 0 to 30 s and is plotted in Fig. 16. There is almost no difference between the results as the local fields are identical.

The mixing index study was done for a bi-disperse system of particles that were initially perfectly mixed in a fluidized bed. The richness index $M_{\phi}$ was applied to the total particle volume fraction to quantify gas-solid mixing. We found that the index captured the presence of low particle volume fraction bubbles well, as shown in Fig. 14. While quantifying the solid-solid mixing with the solid mixing index $M_{\xi_A}$, these bubbles were not visible. The solid fraction field $\xi_A$ and the solid-solid mixing index $M_{\xi_A}$, were found to be almost identical, as shown in Fig. 15. The global average of the solid fraction field $\overline{\xi_A}$ is close to 0.5, and therefore almost no scaling is done by the mixing index. The Rose index was computed for the both the solid fraction field $\xi_A$ and the local solid mixing index field $M_{\xi_A}$, and were shown to be nearly identical as well.

**5. Tunable sensitivity via accessed states**

In a system, the quality of mixing may never be perfectly mixed or segregated. The biomass problem starts with a fully segregated initial state but never reaches a fully mixed state, and vice versa for the

segregation problem. The richness index $M_{\phi}$ and the solid mixing index $M_{\xi_A}$ were applied to both problems using the whole range possible states. That is, the solid volume fraction $\phi$ used was from 0 to the maximum packing limit $\phi_{max}$, and for the solid fraction $\xi_A$ the range from 0 to 1 was used. Realistically, the region of accessed mixing states may be smaller. Defining a mixing index between unrealistic states may obscure the relative levels of mixing or segregation in a system. We therefore introduce a new performance criterion, which we *sensitivity*. A mixing index that can be sensitive to capture these features will provide additional information on the quality of mixing in a system. The local mixing indices derived in section 2 have tunable sensitivity and can be applied to an accessed region. We saw that, by applying the Rose index to the local solid mixing index we improved the sensitivity of the index to initial states of injection in the biomass problem. By tuning the local mixing index further, we may improve the performance of the Rose index.

*5.1. Formulation*

The sensitivity tuning can be done by defining the minimum and maximum limits of the accessed mixing state. The derivation with these limits can then be done by defining the index as:

$$M_{\varphi} = \begin{cases} 0, & \varphi < \varphi_{min} \\ e_1\varphi + f_1, & \varphi_{min} \le \varphi < \bar{\varphi} \\ e_2\varphi + f_2, & \bar{\varphi} \le \varphi \le \varphi_{max} \\ 1, & \varphi > \varphi_{max} \end{cases}, \tag{5.1}$$

where $\varphi$ can be either the solid volume fraction $\phi$ or the solid fraction $\xi$. The coefficients $e_1$, $f_1$, $e_2$, and $f_2$ can be calculated using the following limits:

$$\begin{array}{ll} \varphi = \varphi_{min}, & M_{\varphi} = 0, \\ \varphi = \bar{\varphi}, & M_{\varphi} = 0.5, \\ \varphi = \varphi_{max}, & M_{\varphi} = 1. \end{array} \tag{5.2}$$

The resulting index obtained has the form:

$$M_{\varphi} = \begin{cases} 0, & \varphi < \varphi_{min} \\ \dfrac{\varphi - \varphi_{min}}{2(\bar{\varphi} - \varphi_{min})}, & \varphi_{min} \le \varphi < \bar{\varphi} \\ 1 - \dfrac{\varphi_{max} - \varphi}{2(\varphi_{max} - \bar{\varphi})}, & \bar{\varphi} \le \varphi \le \varphi_{max} \\ 1, & \varphi > \varphi_{max} \end{cases}. \tag{5.3}$$

*5.2. Mixing of biomass and sand*

The local mixing can be fine-tuned further to distinguish the performance of the two designs. Instead

of scaling the solid fraction fields from 0 to 1, we could pick a region within a certain range of values. The average biomass solid fraction is 0.12 for both designs at 10 s. Looking at the solid fraction plots of biomass in Fig. 7, selecting the range of 0.04 to 0.4 is feasible. To compare the two results, both the standard scale and accessed region are given in Fig. 17. The differences between the designs can be seen more clearly: Design 1 has a larger region of well-mixed sand and biomass at 10 s.

As in Fig. 10, the global mixing index can be applied to the accessed solid mixing index. The two ranges are plotted in Fig. 18 for time 1 s to 10 s. The average biomass increases as it is injected into the bed. The minimum solid fraction was set to 0, but the maximum solid fraction was set to 0.75 and 0.5, respectively. There is an almost undiscernible decrease in the quality of mixing of Design 1, but a discernable reduction in the quality of mixing in Design 2 for initial time of inject, as shown in Fig. 18. The difference in the performance of the index between the designs increases with time as can be seen in Fig. 18. The difference has increased from 18.2 % between the using the maximum solid fraction $\xi_{max}$ of 0.75 to 34.9% with setting maximum solid fraction $\xi_{max}$ to 0.5 at 10 s. The sensitivity of the mixing index has improved.

*5.3. Segregation*

The local accessed solid mixing index can be applied to the solid fraction fields for the segregation problem as well. Majority of the domain has a solid fraction value between 0.3 and 0.7. Two different accessed regions ranges were chosen to compare to the original mixing index. The accessed regions of solid fractions with ranges of 0.2 to 0.8 and 0.3 to 0.7 are computed as shown in Fig. 19. To compare these results, the color bar range of 0 to 1 is used. By computing the mixing index of the accessed region, the index's sensitivity can be tuned, and the regions of mixing can be discerned.

The global mixing index is applied to the accessed solid mixing index, as shown in Fig. 20. The sensitivity of accessed regions is captured by the global mixing index. The results change more dramatically in contrast to the biomass problem.

Accessed regions of solid fraction $\xi_A$ were chosen in both the biomass and segregation problem, and the spatial representation were enhanced in both cases. More details in local mixing or segregation were captured as shown in Fig. 17 for the biomass problem, and in Fig. 19 for the segregation case. However, we found that the sensitivity had a larger effect on the performance of the Rose index in the segregation problem in contrast to the biomass problem.

## 6. Discussion

Local mixing indices which are a function of space, characterize spatial mixing patterns in a device through their spatial dependence. On the other hand, global mixing indices provide a single scalar value that is a metric for the quality of mixing of the system in its entirety. The purpose of local mixing indices is to identify regions of rich, lean, and well mixedness in a device, while the global mixing indices are useful for comparing designs. Local mixing indices are computationally inexpensive and can be applied to volume fraction fields obtained from CFD simulations or X-ray computed tomography (XCT) experiments. A grid of sampling volumes can be constructed and used to compute both local and global indices. Note that the sampling grid need not be the same as the computational grid. The global average of the solid volume fractions and the solid fraction is computed from this grid by taking the sample mean of the corresponding values at each sampling volume. Then the formulations given by Eq. (2.5), Eq. (2.10), and Eq. (5.3) can be applied to calculate the richness index, solid mixing index, and accessed region mixing index, respectively, at each sampling volume grid location. The variance or standard deviation can be calculated from the sampling volumes, and the global indices of Lacey or Rose, respectively, can be calculated for the device.

The performance of the mixing index was characterized in two applications of fluidized bed. The first is the mixing of biomass and sand in a reactor designed for biomass fast pyrolysis. The second is the segregation of a binary mixture of particles with similar densities but different sizes. Although the two problems are solved with the same set of equations, there are important differences in the mixing characteristics. The initial conditions of the two problems correspond to the two extremes of the mixing problem. In the biomass problem, the two types of particles are initially fully segregated. Biomass is injected into the fluidized bed where it mixes with sand. In the segregation problem the two particles are perfectly mixed initially and begin to segregate as the bed is fluidized.

The quantity of particles in the segregation problem remains constant in time, while the amount of biomass increases as it is injected into the bed. The global average of biomass changes with time in the biomass problem, while that of the particles in the segregation problem is constant. This is important because the mixing indices are computed using global averages. For the richness index, the global average of solid volume fraction $\phi$ corresponds to perfect gas-solid mixing, and the global average of solid fraction $\xi$ corresponds to perfect solid-solid mixing. Therefore, the average solid volume fraction $\bar{\phi}$, and average solid fractions of biomass $\bar{\xi}_A$, need to be calculated for each time-step in the biomass problem. However, note that only the average solid fraction $\bar{\xi}_A$ needs to be computed

for each time-step in the segregation problem. The novelty in using the local mixing indices $M_{\phi}$ and $M_{\xi_A}$, is that the solid volume fraction and solid fraction fields are scaled by mapping of the global averages to 0.5, thereby removing any dependence on the global average. In addition to quantifying spatial mixing, the benefit of the new index $M_{\xi_A}$ is that the performance of the Rose index was improved when used with the local solid mixing index $M_{\xi_A}$ rather than using the solid fraction $\xi_A$, showing that the difference between the designs was more significant, and the mixing improves for the initial time as the biomass is injected in the bed.

The presence of bubbles with solid volume fraction of order 0.01 are observed in the Design with higher injection inlet in the biomass case and the 2D segregation case. Unlike granular mixing, where the total solid volume fraction does not vary appreciably in the domain, in gas-solid problems, the total solid volume fraction can range from zero to its maximum value in regions of maximum solid packing. The solid fractions do not capture the effects of the bubbles, as they compute the relative proportion of a type of particle in a mixture of particles. Therefore, in gas-solid problems, the local solid fraction alone does not provide a good indication of solid-solid mixing throughout the domain. Both richness and solid fraction mixing indices are needed to characterize solid-solid mixing in gas-solid flows. In addition, a conditional solid mixing index is needed to account for the effect of bubbles when studying solid-solid mixing.

The sensitivity of the local mixing indices can be enhanced by performing a re-scaling of solid volume fraction and solid fraction fields in an accessed region. The mixing index was computed on the solid fraction field for both applications, and the sensitivity of this local mixing index was shown to improve in both cases. The differences in performance of the two designs in the biomass problem are easier to discern, and the local regions in the segregation were better captured. However, it is important to note that choosing the accessed regions depends on the problem under consideration. The global mixing index was applied to these accessed region fields. While there was only a slight improvement in the sensitivity of the global mixing index in the biomass problem, there was a substantial effect on the index's performance in the segregation problem. The Lacey index characterizes the departure of the variance of the current sample state from a reference unmixed state, scaled by the difference in the variance between perfectly mixed and unmixed reference states. These reference states correspond to a reference distribution*. Other distributions could be used as the reference distributions for the

*The term distribution here is not used in the strict sense of the word, as in probability distribution.*

unmixed and perfectly mixed states, resulting in a more sensitive index.

In this study, the mixing indices were computed directly on the computational grid; therefore, the sampling volume was the same as the size of the cell volumes from the CFD simulations. The solid volume fraction fields obtained from the simulations can be sampled with larger volumes by mapping the results to grids with desired cell sizes. If the length scale of the sampling volume is smaller than the smallest length scale of the solid volume fraction, the results are expected to be grid-independent. If larger sampling volumes are used, micro-mixing features with a length scale smaller than the sampling volume will be excluded. Mixing can vary depending on the scale at which the system is observed. Therefore, a mixing index that can capture mixing at different scales by using larger sampling volumes can be devised.

**7. Summary**

Conventional mixing indices are based on realizations of particle data obtained from DEM simulations or experiments. They cannot be applied as-is to average solid volume fraction fields obtained from E-E multi-fluid model simulations or XCT experiments. In this paper, we develop and present two new mixing indices for gas-solid mixing based on average solid volume fraction fields. These mixing indices are the richness mixing index that characterizes gas-solid mixing, and the solid fraction mixing index that characterizes solid-solid mixing.

The richness index, $M_{\phi}$, is analogous to the mixture fraction that arises in single-phase mixing of fuel and oxidizer in combustion problems. It employs a local linear transformation that normalizes gas-solid mixing characteristics in different spatial regions by eliminating dependence on the global average of the total solid volume fraction. Therefore, the richness mixing index, which always lies between 0 (pure gas) and 1 (fully packed solids), indicates the local departure from perfect mixing corresponding to 0.5. Perfect mixing corresponds to the local total solid volume fraction being equal to the global average total solid volume fraction. The solid fraction mixing index, $M_{\xi_A}$, employs a similar idea and normalizes solid-solid mixing characteristics in different spatial regions by eliminating dependence on the global average of the solid fraction of individual solid particle types. It also always lies between 0 (absence of particle A) and 1 (only particle A is present), indicating the local departure from perfect mixing corresponding to 0.5. Perfect solid-solid mixing corresponds to the local solid fraction of A being equal to the global average solid fraction of A.

These mixing indices are local in the sense of capturing spatial mixing patterns in a device. They are

intended to be applied to sampling volumes that are smaller than the smallest length scales of the average volume fraction fields, which in turn are obtained from mesh-converged simulations. In this range of sampling volumes, these local mixing indices are expected to be independent of the sampling volume itself; that is, the local mixing indices within this range are grid-independent. The term grid-independence is strictly used in the context of computing a mixing index and is not the same as mesh-convergence for computational fluid dynamics.

The mixing indices were applied directly on the computational grid of two different applications in fluidized beds. The first application is the mixing of biomass and sand in a fluidized bed reactor designed for fast pyrolysis. The mixing patterns for two different designs are evaluated to determine whether a higher or lower injection location for the biomass yields better mixing of biomass and sand. The local mixing indices show that the design with a lower injection inlet result in better overall mixing. In the second application, two-dimensional simulations were performed of an initially perfectly mixed binary mixture of particles leading to segregation. Low volume fraction bubbles are seen in the segregation problem and in Design 2 in the biomass case, but not in Design 1. The current formulation of the solid-solid mixing index does not account for the presence of bubbles. Both richness and solid fraction mixing indices are needed to characterize solid-solid mixing in gas-solid flows.

It is useful to have a single scalar measure of mixing that can be used to evaluate different designs. Global indices that provide a single scalar measure of mixing in a system can be derived from these local mixing indices by extending variance-based or standard deviation-based indices, originally developed for particle mixing by Lacey and Rose, respectively. Considerable improvement in the representation of time-evolution of mixing is observed when using the global Rose solid fraction mixing index $M_{\xi_A}$, as opposed to a global Rose solid fraction index. This justifies the development of the solid fraction mixing index, as opposed to simply using Rose's index based on the solid fraction and emphasizes the importance of normalizing the departure from the mixed state in different spatial regions.

Sensitivity of a mixing index is a new performance criterion introduced in this work. A global index that is sensitive to design changes can be useful for making design decisions. The sensitivity of global indices based on standard deviation or variance of the local solid fraction mixing index depends on two factors: (a) the sensitivity of the local mixing index and (b) choice of the reference distribution corresponding to the perfectly mixed and perfectly unmixed states. The local mixing indices developed in this paper have tunable sensitivity. The newly developed mixing indices allow the first sensitivity

factor to be tuned by introducing the concept of accessed regions, namely, by recognizing that only a portion of the range of solid volume fraction (for richness) or solid fraction (for solid-solid mixing) values are accessed in a particular application.

## 8. Conclusions

In this paper, we develop and present two new mixing indices for gas-solid and solid-solid mixing based on average solid volume fraction fields in gas-solid flows. These new indices employ a local linear transformation that normalizes mixing characteristics in different spatial regions by eliminating dependence on the global average of the total solid volume fraction in gas-solid mixing and total solid fraction in solid-solid mixing. Significant improvement in the performance of the global Rose index is observed when formulated based on solid fraction mixing index $M_{\xi_A}$, as opposed to a global Rose solid fraction index. Finally, the newly developed mixing indices have tunable sensitivity by introducing the concept of accessed regions.

## Acknowledgments

This material is based upon work supported by the U.S. Department of Energy's Office of Energy Efficiency and Renewable Energy (EERE) under the Advanced Manufacturing Office Award Number DE-EE0008326.

The Authors would like to thank the project managers of the US-DOE AMO program, John Winkel and Brian Valentine, as well as Prof. Robert Brown of the Bioeconomy Institute at Iowa State University, for their valuable feedback on the work and results in this article.

necessarily state or reflect those of the United States Government or any agency thereof.

**References**


1. Adanez J, Abad A, Garcia-Labiano F, Gayan P, de Diego LF. Progress in Chemical-Looping Combustion and Reforming technologies. *Prog Energy Combust Sci.* 2012;38(2):215-282. doi:10.1016/j.pecs.2011.09.001

2. Mahalatkar K, Kuhlman J, Huckaby ED, O'Brien T. CFD simulation of a chemical-looping fuel reactor utilizing solid fuel. *Chem Eng Sci.* 2011;66(16):3617-3627. doi:10.1016/j.ces.2011.04.025

3. Bridgwater AV. Principles and practice of biomass fast pyrolysis processes for liquids. *J Anal Appl Pyrolysis.* 1999;51(1):3-22. doi:10.1016/S0165-2370(99)00005-4

4. Bridgwater AV, Meier D, Radlein D. An overview of fast pyrolysis of biomass. *Org Geochem.* 1999;30(12):1479-1493. doi:10.1016/S0146-6380(99)00120-5

5. Yates JG, Simons SJR. Experimental methods in fluidization research. *Int J Multiph Flow.* 1994;20:297-330. doi:10.1016/0301-9322(94)90076-0

6. Chaouki J, Larachi F, Duduković MP. Noninvasive Tomographic and Velocimetric Monitoring of Multiphase Flows. *Ind Eng Chem Res.* 1997;36(11):4476-4503. doi:10.1021/ie970210t

7. Boyer C, Duquenne AM, Wild G. Measuring techniques in gas–liquid and gas–liquid–solid reactors. *Chem Eng Sci.* 2002;57(16):3185-3215. doi:10.1016/S0009-2509(02)00193-8

8. Makkawi YT, Wright PC. Fluidization regimes in a conventional fluidized bed characterized by means of electrical capacitance tomography. *Chem Eng Sci.* 2002;57(13):2411-2437. doi:10.1016/S0009-2509(02)00138-0

9. Makkawi YT, Wright PC. Electrical capacitance tomography for conventional fluidized bed measurements—remarks on the measuring technique. *Powder Technol.* 2004;148(2):142-157. doi:10.1016/j.powtec.2004.09.006

10. Toye D, Fransolet E, Simon D, Crine M, L'Homme G, Marchot P. Possibilities and Limits of Application of Electrical Resistance Tomography in Hydrodynamics of Bubble Columns. *Can J Chem Eng.* 2005;83(1):4-10. doi:https://doi.org/10.1002/cjce.5450830103

11. Mudde RF, Bruneau PRP, van der Hagen THJJ. Time-Resolved γ-Densitometry Imaging within Fluidized Beds. *Ind Eng Chem Res.* 2005;44(16):6181-6187. doi:10.1021/ie049091p

12. Tortora PR, Ceccio SL, O'Hern TJ, Trujillo SM, Torczynski JR. Quantitative measurement of solids distribution in gas–solid riser flows using electrical impedance tomography and gamma densitometry tomography. *Int J Multiph Flow.* 2006;32(8):972-995. doi:10.1016/j.ijmultiphaseflow.2006.03.004

13. Franka NP, Heindel TJ. Local time-averaged gas holdup in a fluidized bed with side air injection using X-ray computed tomography. *Powder Technol.* 2009;193(1):69-78.

doi:10.1016/j.powtec.2009.02.008

14. Mudde RF. Double X-ray Tomography of a Bubbling Fluidized Bed. *Ind Eng Chem Res.* 2010;49(11):5061-5065. doi:10.1021/ie901537z

15. Mudde RF. Time-resolved X-ray tomography of a fluidized bed. *Powder Technol.* 2010;199(1):55-59. doi:10.1016/j.powtec.2009.04.021

16. Heindel TJ. A Review of X-Ray Flow Visualization With Applications to Multiphase Flows. *J Fluids Eng.* 2011;133(074001). doi:10.1115/1.4004367

17. Kingston TA, Geick TA, Robinson TR, Heindel TJ. Characterizing 3D granular flow structures in a double screw mixer using X-ray particle tracking velocimetry. *Powder Technol.* 2015;278:211-222. doi:10.1016/j.powtec.2015.02.061

18. Ketterhagen WR, Curtis JS, Wassgren CR, Hancock BC. Predicting the flow mode from hoppers using the discrete element method. *Powder Technol.* 2009;195(1):1-10. doi:10.1016/j.powtec.2009.05.002

19. Chandratilleke GR, Yu AB, Stewart RL, Bridgwater J. Effects of blade rake angle and gap on particle mixing in a cylindrical mixer. *Powder Technol.* 2009;193(3):303-311. doi:10.1016/j.powtec.2009.03.007

20. Chandratilleke GR, Zhou YC, Yu AB, Bridgwater J. Effect of Blade Speed on Granular Flow and Mixing in a Cylindrical Mixer. *Ind Eng Chem Res.* 2010;49(11):5467-5478. doi:10.1021/ie901581t

21. Jiang M, Zhao Y, Liu G, Zheng J. Enhancing mixing of particles by baffles in a rotating drum mixer. *Particuology.* 2011;9(3):270-278. doi:10.1016/j.partic.2010.06.008

22. Hua X, Curtis J, Hancock B, Ketterhagen W, Wassgren C. The kinematics of non-cohesive, sphero-cylindrical particles in a low-speed, vertical axis mixer. *Chem Eng Sci.* 2013;101:144-164. doi:10.1016/j.ces.2013.05.063

23. Chandratilleke R, Yu A, Bridgwater J, Shinohara K. Flow and Mixing of Cohesive Particles in a Vertical Bladed Mixer. *Ind Eng Chem Res.* 2014;53(10):4119-4130. doi:10.1021/ie403877v

24. Alian M, Ein-Mozaffari F, Upreti SR. Analysis of the mixing of solid particles in a plowshare mixer via discrete element method (DEM). *Powder Technol.* 2015;274:77-87. doi:10.1016/j.powtec.2015.01.012

25. Takabatake K, Mori Y, Khinast JG, Sakai M. Numerical investigation of a coarse-grain discrete element method in solid mixing in a spouted bed. *Chem Eng J.* 2018;346:416-426. doi:10.1016/j.cej.2018.04.015

26. Chandratilleke GR, Dong KJ, Shen YS. DEM study of the effect of blade-support spokes on mixing performance in a ribbon mixer. *Powder Technol.* 2018;326:123-136. doi:10.1016/j.powtec.2017.12.055

27. Govender N, Wilke DN, Wu CY, Rajamani R, Khinast J, Glasser BJ. Large-scale GPU based DEM modeling of mixing using irregularly shaped particles. *Adv Powder Technol.* 2018;29(10):2476-2490. doi:10.1016/j.apt.2018.06.028

28. Liu R, Zhou Z, Xiao R, Yu A. CFD-DEM modelling of mixing of granular materials in multiple jets fluidized beds. *Powder Technol.* 2020;361:315-325. doi:10.1016/j.powtec.2019.08.002

29. Li S, Kajiwara S, Sakai M. Numerical investigation on the mixing mechanism in a cross-torus paddle mixer using the DEM-CFD method. *Powder Technol.* 2021;377:89-102. doi:10.1016/j.powtec.2020.08.085

30. Jenkins JT, Mancini F. Kinetic theory for binary mixtures of smooth, nearly elastic spheres. *Phys Fluids Fluid Dyn.* 1989;1(12):2050-2057. doi:10.1063/1.857479

31. Syamlal M, Rogers W, O`Brien TJ. *MFIX Documentation Theory Guide*. USDOE Morgantown Energy Technology Center, WV (United States); 1993. doi:10.2172/10145548

32. Drew DA. Mathematical Modeling of Two-Phase Flow. *Annu Rev Fluid Mech.* 1983;15(1):261-291. doi:10.1146/annurev.fl.15.010183.001401

33. Pai MG, Subramaniam S. A comprehensive probability density function formalism for multiphase flows. *J Fluid Mech.* 2009;628:181-228. doi:10.1017/S002211200900617X

34. Jenkins JT, Savage SB. A theory for the rapid flow of identical, smooth, nearly elastic, spherical particles. *J Fluid Mech.* 1983;130:187-202. doi:10.1017/S0022112083001044

35. Jenkins JT, Mancini F. Balance Laws and Constitutive Relations for Plane Flows of a Dense, Binary Mixture of Smooth, Nearly Elastic, Circular Disks. *J Appl Mech.* 1987;54(1):27-34. doi:10.1115/1.3172990

36. Dahl SR, Hrenya CM, Garzó V, Dufty JW. Kinetic temperatures for a granular mixture. *Phys Rev E.* 2002;66(4):041301. doi:10.1103/PhysRevE.66.041301

37. Garzó V, Hrenya CM, Dufty JW. Enskog theory for polydisperse granular mixtures. II. Sonine polynomial approximation. *Phys Rev E.* 2007;76(3):031304. doi:10.1103/PhysRevE.76.031304

38. Johnson PC, Jackson R. Frictional–collisional constitutive relations for granular materials, with application to plane shearing. *J Fluid Mech.* 1987;176:67-93. doi:10.1017/S0022112087000570

39. Srivastava A, Sundaresan S. Analysis of a frictional–kinetic model for gas–particle flow. *Powder Technol.* 2003;129(1):72-85. doi:10.1016/S0032-5910(02)00132-8

40. Schneiderbauer S, Aigner A, Pirker S. A comprehensive frictional-kinetic model for gas–particle flows: Analysis of fluidized and moving bed regimes. *Chem Eng Sci.* 2012;80:279-292. doi:10.1016/j.ces.2012.06.041

41. Gidaspow D. *Multiphase Flow and Fluidization: Continuum and Kinetic Theory Descriptions with Applications / Dimitri Gidaspow*. Academic Press; 1994.

42. Wen CY, Yu YH. A generalized method for predicting the minimum fluidization velocity. *AIChE J*. 1966;12(3):610-612. doi:https://doi.org/10.1002/aic.690120343

43. ERGUN S. Fluid flow through packed columns. *Chem Eng Prog*. 1952;48:89-94.

44. Tenneti S, Garg R, Subramaniam S. Drag law for monodisperse gas–solid systems using particle-resolved direct numerical simulation of flow past fixed assemblies of spheres. *Int J Multiph Flow*. 2011;37(9):1072-1092. doi:10.1016/j.ijmultiphaseflow.2011.05.010

45. Williams JC. The mixing of dry powders. *Powder Technol*. 1968;2(1):13-20. doi:10.1016/0032-5910(68)80028-2

46. Weidenbaum SS. Mixing of Solids. In: Drew TB, Hoopes JW, eds. *Advances in Chemical Engineering*. Vol 2. Academic Press; 1958:209-324. doi:10.1016/S0065-2377(08)60229-X

47. Fan LT, Chen SJ, Watson CA. ANNUAL REVIEW Solids Mixing. *Ind Eng Chem*. 1970;62(7):53-69. doi:10.1021/ie50727a009

48. Bridgwater J. Fundamental powder mixing mechanisms. *Powder Technol*. 1976;15(2):215-236. doi:10.1016/0032-5910(76)80051-4

49. Fan LT, Chen Y ming, Lai FS. Recent developments in solids mixing. *Powder Technol*. 1990;61(3):255-287. doi:10.1016/0032-5910(90)80092-D

50. Poux M, Fayolle P, Bertrand J, Bridoux D, Bousquet J. Powder mixing: Some practical rules applied to agitated systems. *Powder Technol*. 1991;68(3):213-234. doi:10.1016/0032-5910(91)80047-M

51. Bridgwater J. Mixing of powders and granular materials by mechanical means—A perspective. *Particuology*. 2012;10(4):397-427. doi:10.1016/j.partic.2012.06.002

52. Godlieb W, Gorter S, Deen NG, Kuipers J a. M. DEM and TFM simulations of solids mixing in gas-solid fluidized bed. *Proc 7th Int Conf Comput Fluid Dyn Miner Process Ind CFD 2009 9-11 Dec 2009 Melb Aust*. Published online 2010:097GOD-1/7.

53. Siraj MS, Radl S, Glasser BJ, Khinast JG. Effect of blade angle and particle size on powder mixing performance in a rectangular box. *Powder Technol*. 2011;211(1):100-113. doi:10.1016/j.powtec.2011.04.004

54. Chandratilleke GR, Yu AB, Bridgwater J, Shinohara K. A particle-scale index in the quantification of mixing of particles. *AIChE J*. 2012;58(4):1099-1118. doi:https://doi.org/10.1002/aic.12654

55. Keller NKG, Bai W, Fox RO, Heindel TJ. Quantifying mixing in 3D binary particulate systems. *Chem Eng Sci*. 2013;93:412-422. doi:10.1016/j.ces.2013.01.069

56. Bhalode P, Ierapetritou M. A review of existing mixing indices in solid-based continuous blending operations. *Powder Technol*. 2020;373:195-209. doi:10.1016/j.powtec.2020.06.043

57. Lacey PMC. Developments in the theory of particle mixing. *J Appl Chem*. 1954;4(5):257-268. doi:10.1002/jctb.5010040504

58. Kramer HA (Harold A, United States. Agricultural Research Service. *Effect of Grain Velocity and Flow Rate upon the Performance of a Diverter-Type Sampler*. Washington, D.C.: U.S. Dept. of Agriculture, Agricultural Research Service; 1968. Accessed December 31, 2020. http://archive.org/details/effectofgrainvel25kram

59. Deen NG, Willem G, Sander G, Kuipers JAM. Numerical Analysis of Solids Mixing in Pressurized Fluidized Beds. *Ind Eng Chem Res*. 2010;49(11):5246-5253. doi:10.1021/ie9014843

60. Radl S, Kalvoda E, Glasser BJ, Khinast JG. Mixing characteristics of wet granular matter in a bladed mixer. *Powder Technol*. 2010;200(3):171-189. doi:10.1016/j.powtec.2010.02.022

61. Basinskas G, Sakai M. Numerical study of the mixing efficiency of a batch mixer using the discrete element method. *Powder Technol*. 2016;301:815-829. doi:10.1016/j.powtec.2016.07.017

62. Wen Y, Liu M, Liu B, Shao Y. Comparative Study on the Characterization Method of Particle Mixing Index Using DEM Method. *Procedia Eng*. 2015;102:1630-1642. doi:10.1016/j.proeng.2015.01.299

63. OpenFOAM. The OpenFOAM Foundation. Published 2020. http://openfoam.org/

64. OpenCFD. OpenFOAM v2006 - New OpenQBMM community module. Published 2020. https://www.openfoam.com/releases/openfoam-v2006/numerics.php#numerics-OpenQBMM

65. Polin JP, Peterson CA, Whitmer LE, Smith RG, Brown RC. Process intensification of biomass fast pyrolysis through autothermal operation of a fluidized bed reactor. *Appl Energy*. 2019;249:276-285. doi:10.1016/j.apenergy.2019.04.154

66. Proano‐Aviles J, Lindstrom JK, Johnston PA, Brown RC. Heat and Mass Transfer Effects in a Furnace-Based Micropyrolyzer. *Energy Technol*. 2017;5(1):189-195. doi:https://doi.org/10.1002/ente.201600279

67. Kim KH, Bai X, Rover M, Brown RC. The effect of low-concentration oxygen in sweep gas during pyrolysis of red oak using a fluidized bed reactor. *Fuel*. 2014;124:49-56. doi:10.1016/j.fuel.2014.01.086

68. Sweby P. High resolution schemes using flux limiters for hyperbolic conservation laws. *SIAM J Numer Anal*. 1984;21(5):995-1011. doi:10.1137/0721062

69. Procedure for Estimation and Reporting of Uncertainty Due to Discretization in CFD Applications. *J Fluids Eng*. 2008;130(078001). doi:10.1115/1.2960953

70. Marzocchella A, Salatino P, Pastena VD, Lirer L. Transient fluidization and segregation of binary mixtures of particles. *AIChE J*. 2000;46(11):2175-2182. doi:10.1002/aic.690461110

AIChE Journal
DOI10.1002/aic.17639



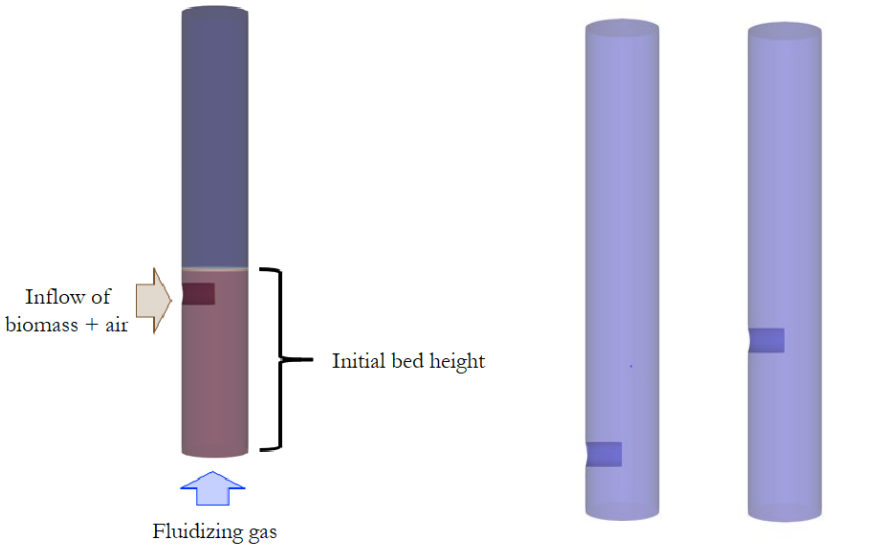


*Computational domain* *Design 1* *Design 2*

*Fig. 1: Geometry of fluidized bed reactor used for autothermal pyrolysis of biomass.*

AIChE Journal
DOI10.1002/aic.17639



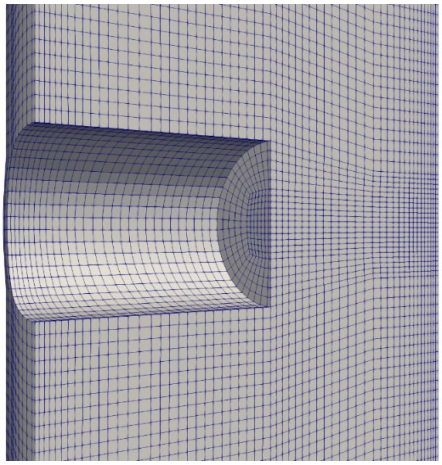

*Injection auger*

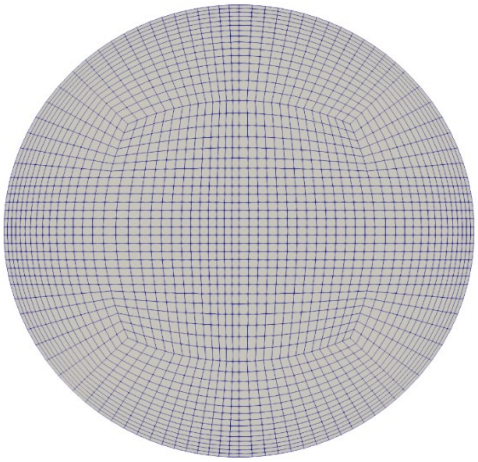

*Reactor cross-section*

*Fig. 2: Computational grid*

AIChE Journal
DOI10.1002/aic.17639

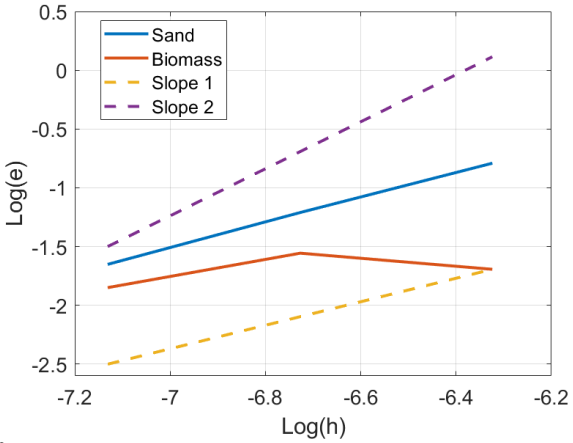


*Fig. 3: $L^2$ norm of the true error of meshes 2,3 and, 4 with respect to mesh 1.*

AIChE Journal
DOI10.1002/aic.17639

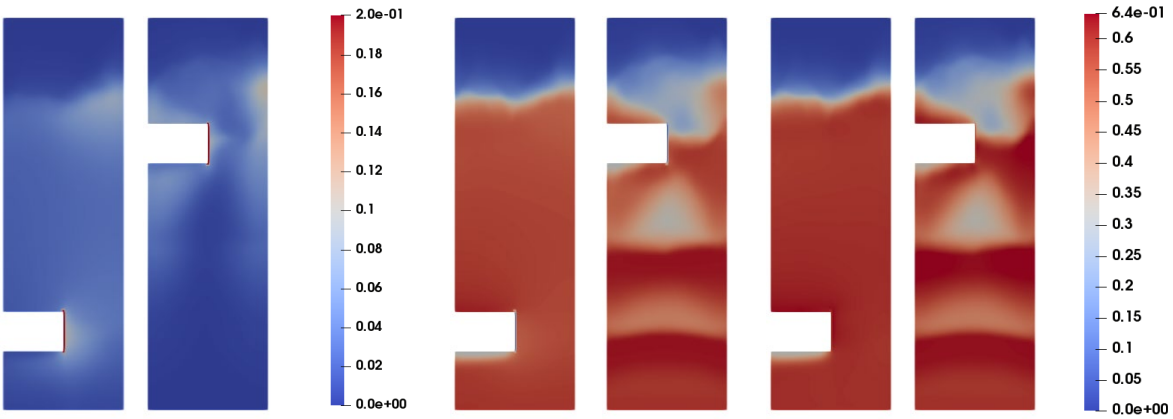


*Design 1* *Design 2* *Design 1* *Design 2* *Design 1* *Design 2*

*Biomass* *Sand* *Total*

*Fig. 4: Volume fraction of biomass $\phi_A$, sand $\phi_B$, and total particles $\phi$ for both designs at 5 s.*

AIChE Journal
DOI10.1002/aic.17639

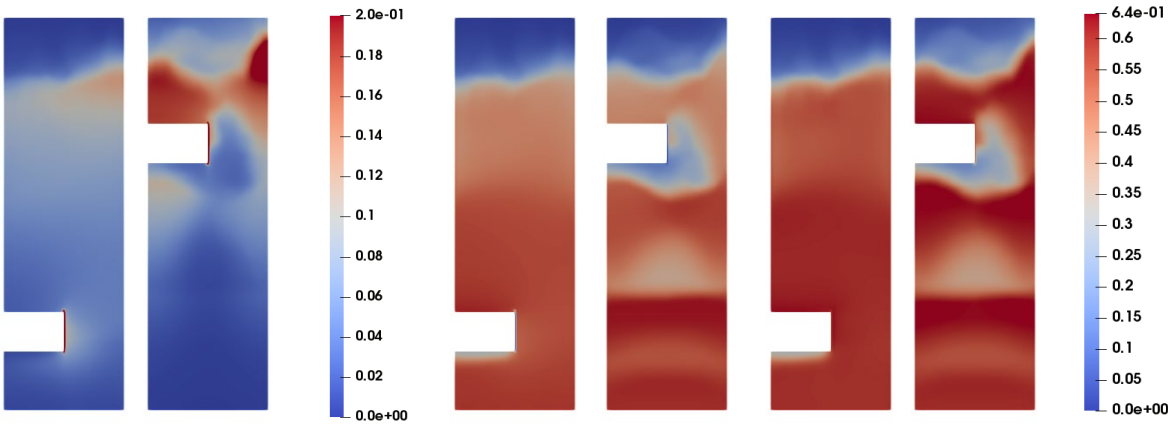


*Design 1* *Design 2* *Design 1* *Design 2* *Design 1* *Design 2*

*Biomass* *Sand* *Total*

*Fig. 5: Volume fraction of biomass $\phi_A$, sand $\phi_B$, and total particles $\phi$ for both designs at 10 s.*

AIChE Journal
DOI10.1002/aic.17639

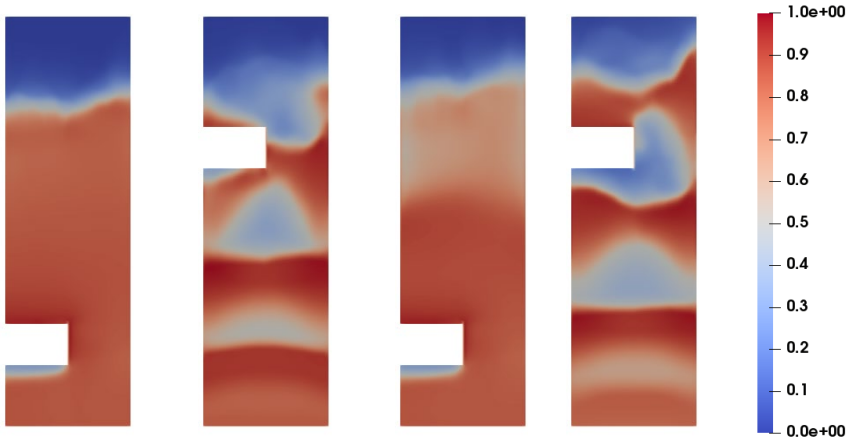


*Fig. 6: Richness index $M_\phi$ of total particles for both designs at 5 and 10 s.*

AIChE Journal
DOI10.1002/aic.17639



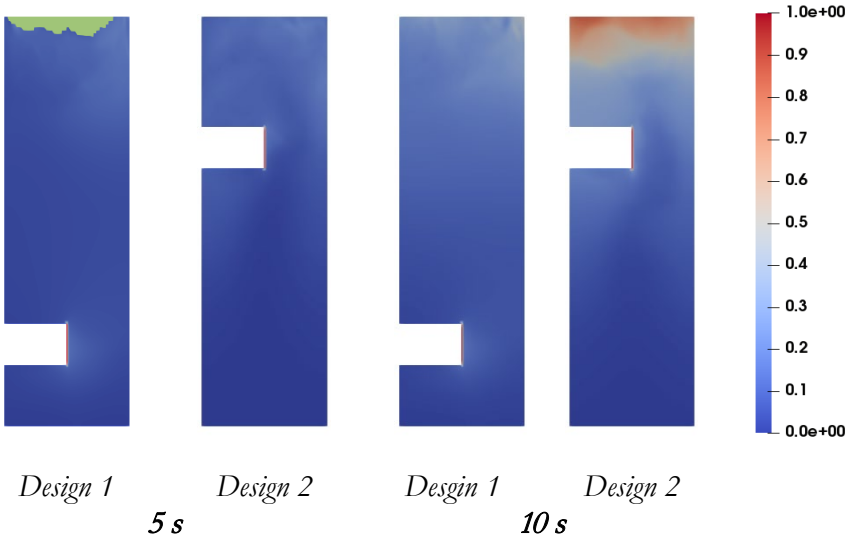


*Fig. 7: Solid fraction of biomass $\xi_A$ for both designs at 5 and 10 s. The green region at the top of the plot at 5 s represents an undefined solid fraction.*

AIChE Journal
DOI10.1002/aic.17639




*Fig. 8: Mixing index of biomass $M_{\xi_A}$ for both designs at 5 and 10 s. The green region at the top of the plot at 5 s represents an undefined solid-solid mixing.*

AIChE Journal
DOI10.1002/aic.17639

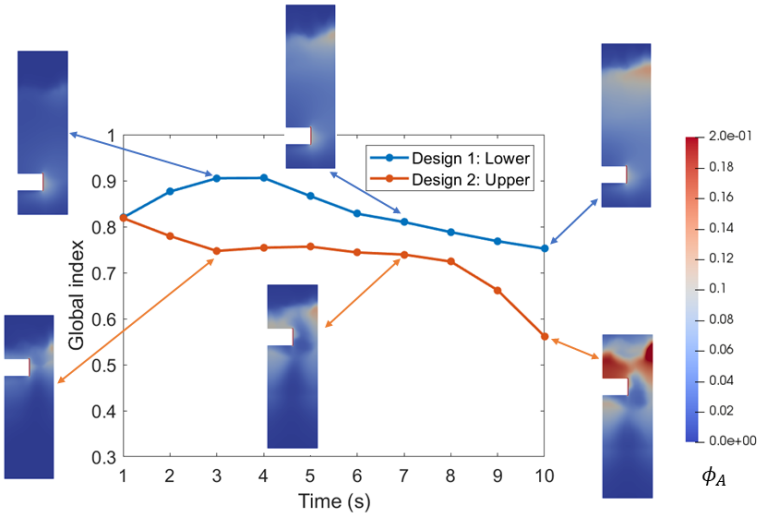


*Fig. 9: Rose index applied to biomass solid fraction* $\xi_A$

AIChE Journal
DOI10.1002/aic.17639

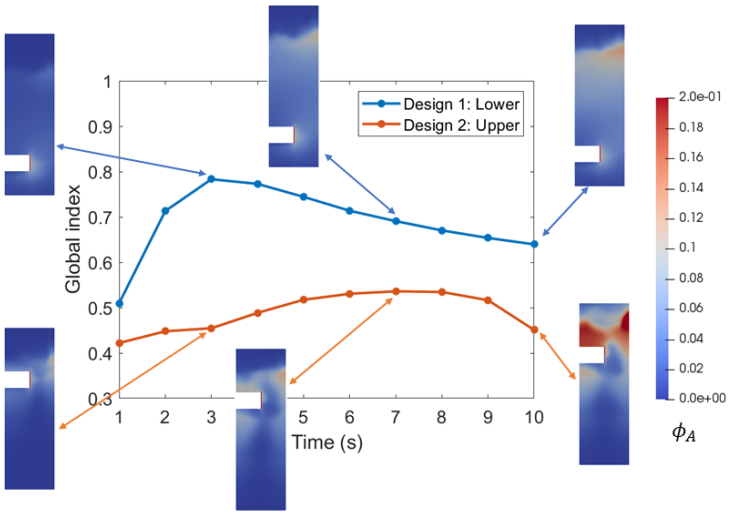


*Fig. 10: Rose index applied to biomass local solid-solid mixing index* $M_{\xi_A}$

AIChE Journal
DOI10.1002/aic.17639



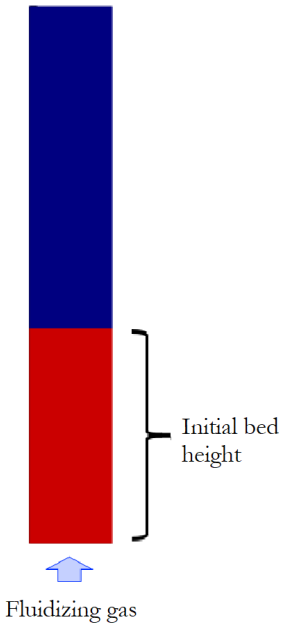


*Fig. 11: Computational domain.*

AIChE Journal
DOI10.1002/aic.17639

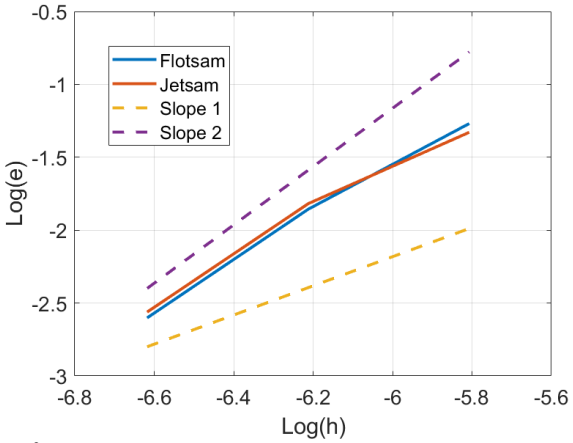


*Fig. 12: $L^2$ norm of true error of meshes 2,3 and, 4 with respect to mesh 1.*

AIChE Journal
DOI10.1002/aic.17639

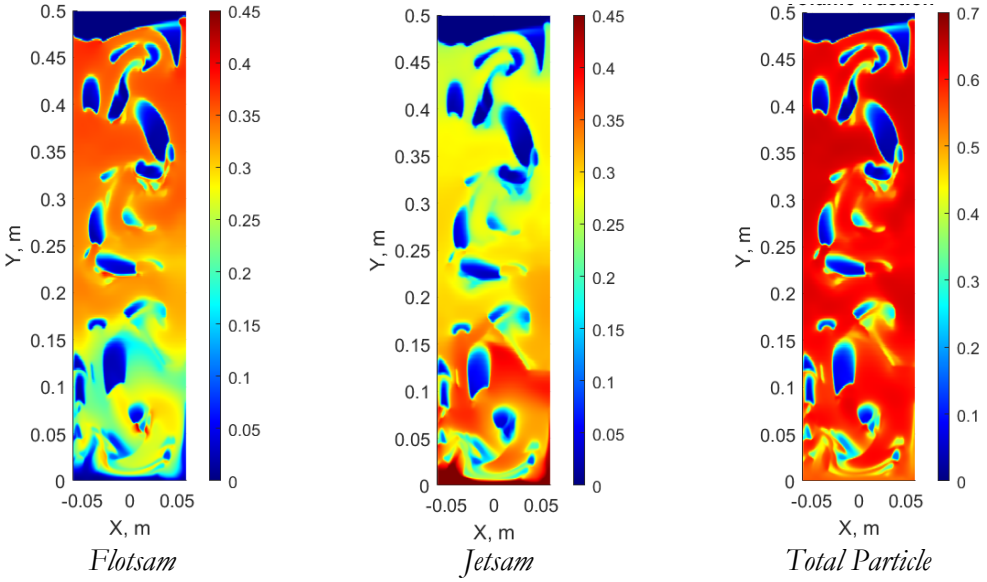


*Fig. 13: Volume fraction of flotsam $\phi_A$, jetsam $\phi_B$, and total particles $\phi$.*

AIChE Journal
DOI10.1002/aic.17639

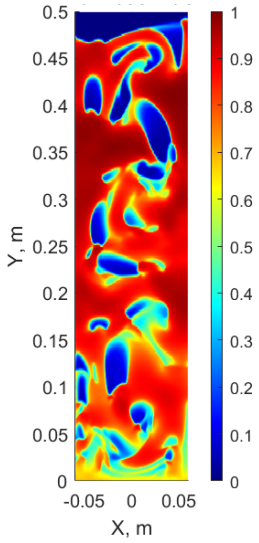


*Fig. 14: Richness index $M_\phi$ applied to total particles.*

AIChE Journal
DOI10.1002/aic.17639



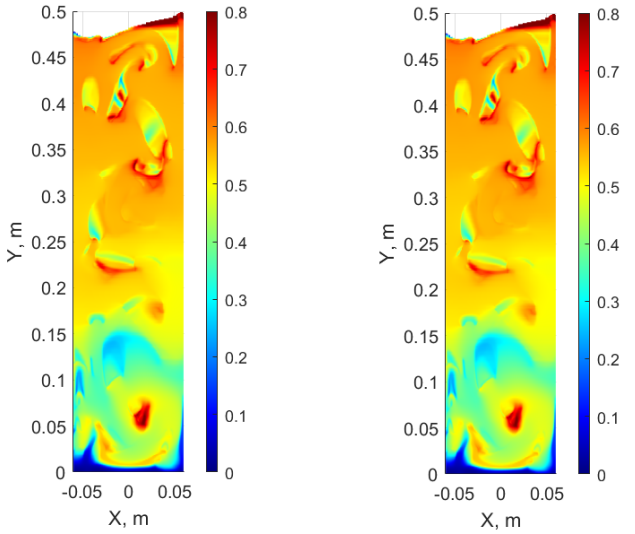


*Solid fraction* $\xi_A$ *Solid mixing index* $M_{\xi_A}$

*Fig. 15: Solid fraction and mixing index of flotsam particles.*

AIChE Journal
DOI10.1002/aic.17639

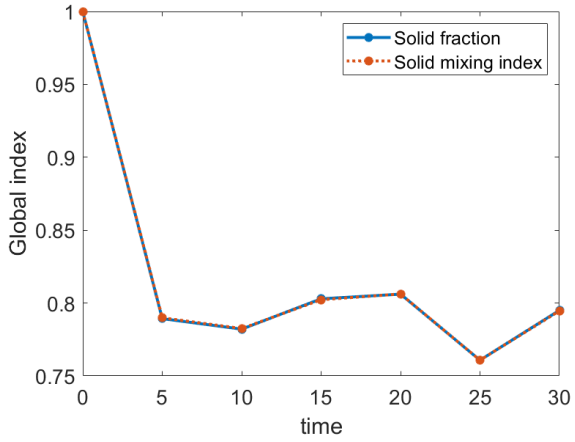


*Fig. 16: Global indices.*

AIChE Journal
DOI10.1002/aic.17639



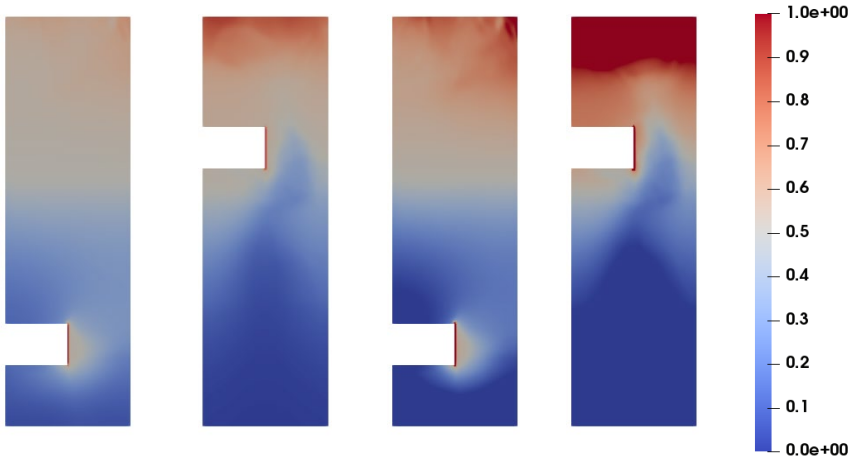


*Fig. 17: Accessed region mixing index of biomass for both designs at 10 s.*

AIChE Journal
DOI10.1002/aic.17639

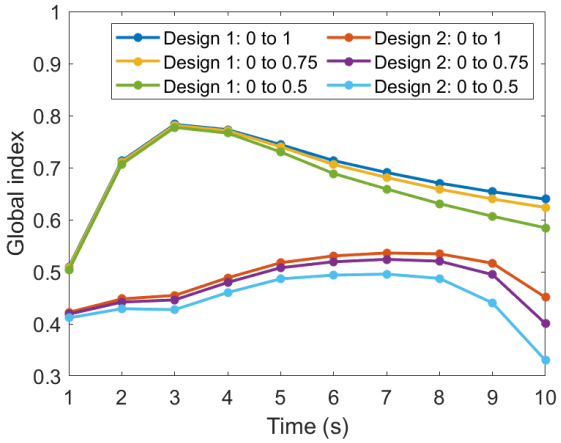


*Fig. 18: Rose index applied to local accessed solid mixing index of biomass.*

AIChE Journal
DOI10.1002/aic.17639

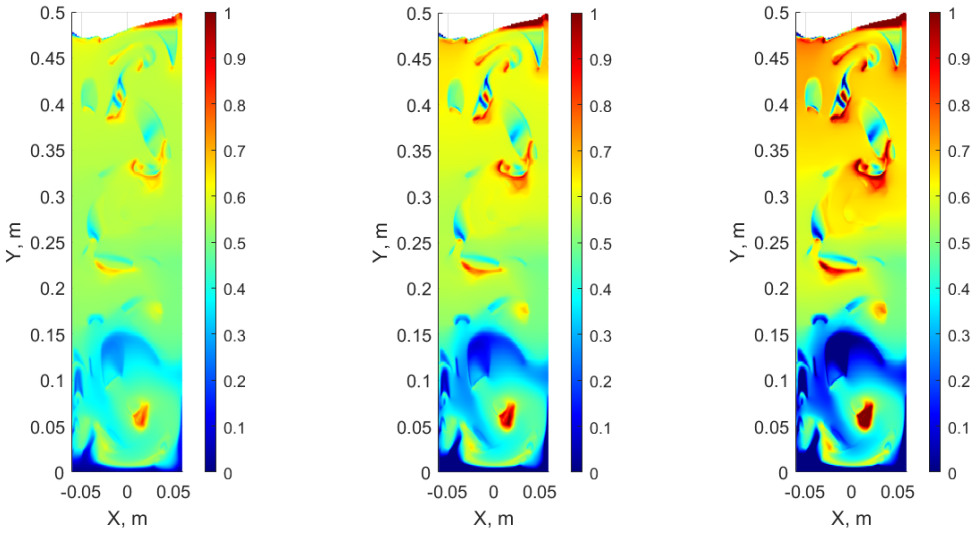


*0 to 1* *0.2 to 0.8* *0.3 to 0.7*

*Fig. 19: Accessed solid mixing index for* $\xi_{min}$ *to* $\xi_{max}$.

AIChE Journal
DOI10.1002/aic.17639

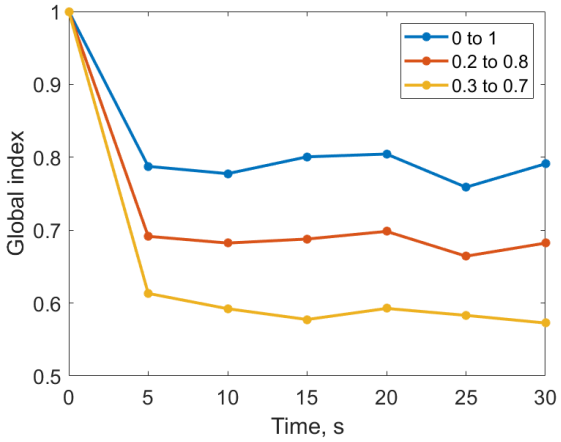


*Fig. 20: Global index applied to accessed regions.*

AIChE Journal
DOI10.1002/aic.17639



*Table 1: Mesh sizes.*

| Mesh | Cells | Mesh size $\boldsymbol{h}$ (mm) |
|---|---|---|
| **1** | 1,813,672 | 0.53345 |
| **2** | 551,381 | 0.80017 |
| **3** | 164,009 | 1.19857 |
| **4** | 49,142 | 1.79356 |

*Table 2: Grid convergence error global index.*

| Property | Sand volume fraction | Biomass volume fraction |
|---|---|---|
| $\emptyset_1$ | 0.6754 | 0.8024 |
| $\emptyset_2$ | 0.6456 | 0.8211 |
| $\emptyset_3$ | 0.6330 | 0.8179 |
| $e_a^{21}$ | 4.44% | 2.33% |
| $GCI_{fine}^{21}$ | 3.96% | 0.6% |
| $p$ | 2.161 | 4.354 |

*Table 3: Properties of the binary mixture[70].*

| Property | Silica sand (Flotsam) | Glass beads (Jetsam) |
|---|---|---|
| Sauter mean diameter [μm] | 125 | 500 |
| Size [μm] | 100-150 | 400-600 |
| Sphericity [-] | 1 | 1 |
| Density [$kg/m^3$] | 2600 | 2540 |
| Geldart group [-] | B | B |
| Terminal velocity [$m/s$] | 0.8 | 4.1 |
| Minimum fluidization velocity [$m/s$] | 0.017 | 0.22 |

*Table 4: Mesh sizes.*

| Mesh | Cells | Mesh size $\boldsymbol{h}$ (mm) |
|---|---|---|
| **1** | 151,200 | 0.891 |
| **2** | 67,200 | 1.336 |
| **3** | 29,840 | 2.00 |
| **4** | 13,197 | 3.00 |

*Table 5: Mesh convergence error global index.*

| Property | Flotsam volume fraction | Jetsam volume fraction |
|---|---|---|
| $\emptyset_1$ | 0.8364 | 0.8543 |
| $\emptyset_2$ | 0.8249 | 0.8450 |
| $\emptyset_3$ | 0.8077 | 0.8313 |
| $e_a^{21}$ | 1.38% | 1.08% |
| $GCI_{fine}^{21}$ | 3.6% | 2.81% |
| $p$ | 0.966 | 0.9705 |